



Ultra-uniform MIL-88B(Fe)/Fe₃S₄ hybrids engineered by partial sulfidation to boost catalysis in electro-Fenton treatment of micropollutants: Experimental and mechanistic insights

Zhihong Ye^a, Wenfeng Zhang^a, Sonia Lanzalaco^b, Lele Zhao^c, Ignasi Sirés^{c,*}, Pan Xia^a, Jun Zhai^a, Qiang He^{a,*}

^a Key Laboratory of Eco-environments in Three Gorges Reservoir Region, Ministry of Education, College of Environment and Ecology, Chongqing University, Chongqing 400045, China

^b Departament d'Enginyeria Química and Barcelona Research Center in Multiscale Science and Engineering, EEBE, Universitat Politècnica de Catalunya, C/Eduard Maristany, 10-14, 08019 Barcelona, Spain

^c Laboratori d'Electroquímica dels Materials i del Medi Ambient, Departament de Ciència de Materials i Química Física, Secció de Química Física, Facultat de Química, Universitat de Barcelona, Martí i Franquès 1-11, 08028 Barcelona, Spain

ARTICLE INFO

Keywords:

Heterogeneous electro-Fenton
Metal-organic framework
Fe(II) regeneration
Pharmaceutical pollution
Water treatment

ABSTRACT

Fe-based metal-organic frameworks are promising catalysts for water treatment, although their viability is hampered by the slow regeneration of active Fe(II) sites. A facile sulfidation strategy is proposed to boost the catalytic activity of MIL-88B(Fe) in heterogeneous electro-Fenton (HEF) treatment of organic micropollutants at mild pH. The synthesized MIL-88B(Fe)/Fe₃S₄ hybrids possessed numerous and durable unsaturated iron sites, acting the S²⁻ atoms as electron donors that enhanced the Fe(II) recycling. The sulfidated catalyst outperformed the MIL-88B(Fe), as evidenced by the 7-fold faster degradation of antibiotic trimethoprim by HEF and the fast destruction of micropollutants in urban wastewater. The hybrid catalyst was reused, obtaining >90% drug removal after four runs and, additionally, its inherent magnetism facilitated the post-treatment recovery. Electrochemical tests and DFT calculations provided mechanistic insights to explain the enhanced catalysis, suggesting that the accelerated Fe(III)/Fe(II) cycling and the enhanced mass transport and electron transfer accounted for the efficient trimethoprim degradation.

1. Introduction

In the last decade, electro-Fenton (EF) has become the most popular among the so-called electrochemical advanced oxidation processes (EAOPs) for the remediation of wastewater containing organic micropollutants like pharmaceuticals, owing to the efficient production of free and highly active hydroxyl radicals ([•]OH, *E*^o = 2.80 V/SHE) via Fenton's reaction (1) [1–3]. In EF, the oxidation is empowered by the simultaneous production of adsorbed [•]OH on the anode from reaction (2) [4]. The utilization of carbonaceous cathodes enables massive in-situ generation of H₂O₂ through the 2-electron oxygen reduction reaction (3), a distinct feature as compared to conventional Fenton process that allows minimizing the negative aspects associated to the industrial H₂O₂ supply chain [3,5,6]. Moreover, the continuous Fe³⁺ reduction from reaction (4) at the cathode maintains the catalytic cycle [7,8].



Nonetheless, the implementation of conventional homogeneous EF at large scale is currently limited by the need of a strict control of solution pH (optimum at ~3) and the gradual deposition of iron mud [9]. The development of heterogeneous electro-Fenton (HEF) process based on the employment of suspended solid catalysts to replace soluble Fe²⁺ salts has mitigate these problems, although new challenges have emerged: (i) irreversible loss of metal active sites due to leaching; (ii) slow regeneration of unsaturated Fe(II) sites because reaction (4)

* Corresponding authors.

E-mail addresses: i.sires@ub.edu (I. Sirés), heqiang@cqu.edu.cn (Q. He).

<https://doi.org/10.1016/j.cej.2022.140757>

Received 13 October 2022; Received in revised form 29 November 2022; Accepted 30 November 2022

Available online 2 December 2022

1385-8947/© 2022 The Authors. Published by Elsevier B.V. This is an open access article under the CC BY-NC-ND license (<http://creativecommons.org/licenses/by-nc-nd/4.0/>).

becomes ineffective; (iii) reduced number of exposed active centers towards H_2O_2 and pollutants, since most of them are embedded inside the 3D structure; and (iv) particle aggregation and deactivation, which limits their recyclability [1,4,10]. H_2O_2 may act as an electron donor to regenerate Fe(II) sites via Fenton-like reaction (5), but this is quite inefficient due to the extremely slow reaction kinetics ($k = 0.001\text{--}0.01 \text{ M}^{-1} \text{ s}^{-1} \ll k = 63 \text{ M}^{-1} \text{ s}^{-1}$ for reaction (1)), eventually causing a drastic decay in the EF performance [11].

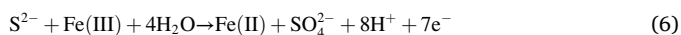


The design of highly porous catalysts accelerates the mass transport of H_2O_2 and pollutants, but also raises the risk of deactivation, leading to low recyclability of catalysts [12–14]. Therefore, breaking the activity-stability trade-off for high performance HEF is still a conundrum to unravel.

Fe-based metal organic frameworks (Fe-MOFs) have been receiving major attention as a new class of catalysts for HEF due to their unique features, arising from a facile synthesis that yields ultraporos and highly tunable structures [15,16]. Among them, MIL-88B(Fe), synthesized by assembling 1,4-benzenedicarboxylic acid ligands and trimeric iron nodes, led to an efficient removal of organic pollutants by HEF, being 10–30-fold quicker than that with simple iron-based catalysts (e. g., iron oxides) [17,18]. The well-developed open pores of MIL-88B(Fe) favor the mass transport of both H_2O_2 and organics to the accessible unsaturated iron active sites, which allows the fast activation of the adsorbed H_2O_2 to yield $\cdot\text{OH}$. Furthermore, the strong coordination of the iron centers minimizes the iron leaching [19,20]. However, an excessive binding of iron centers to organic linkers is detrimental, since it reduces the amount of free active sites for H_2O_2 adsorption and activation. It has been shown that the coordinatively unsaturated iron sites in MIL-88B(Fe) are rather scarce [21], which adds to the slow Fe(II) regeneration, negatively affecting the HEF performance [19,22].

It is thus evident that accelerating the Fe(III)-to-Fe(II) conversion and multiplying the presence of durable unsaturated iron sites are key tasks to enhance the catalytic performance of Fe-MOFs. For this, a first strategy is based on UV/Vis photoirradiation to create electrons at the conduction band of the catalyst, which can be captured by Fe(III), although the efficiency depends on the quantum yield [23]. Alternatively, bimetallic MOFs with partial substitution of iron nodes by other transition metals promote the Fe(II) regeneration via direct electron transfer [24]. Third, the introduction of electrophilic functionalities (e. g., $-\text{NH}_2$) into MIL-88B(Fe) decreases the electron density of iron centers, favoring their reduced form, although such specific ligands may be too expensive [21]. Vacuum activation of MIL-88B(Fe) at 150–250 °C has also been proposed as an alternative approach [19]. On this basis, the quest for facile and cost-effective routes for the synthesis of improved Fe-MOFs catalysts has drawn attention.

Recently, it has been shown that sulfur-doped iron materials accelerate the Fe(III)-to-Fe(II) conversion in non-electrochemical systems [25]. The hybrid molecular orbitals of S-Fe possess larger expansion room, which eases the orbital overlapping between iron sites and H_2O_2 , thereby enhancing the electron transfer from H_2O_2 to Fe(III) required for reaction (5) [22]. Additionally, the unsaturated S atoms can act as electron donors for efficient Fe(III) reduction; for example, up to 7 mol of electrons can be supplied to Fe(III) upon equimolar conversion of S_2^{2-} into SO_4^{2-} (reaction (6)), being more efficient than Fenton-like reaction (5) [10,12].



Iron sulfides as Fenton catalyst experienced a boom in recent years, but they still suffer from low water stability and extremely high iron leaching [10,26]. MIL-100(Fe)-derived Fe_3S_4 exhibited superior catalytic activity for photo-Fenton degradation of sulfonamide antibiotics [27]. Du et al. prepared an S-modified MIL-53(Fe) by calcination of a mixture of MIL-53(Fe) with S, proven to be an efficient EF catalyst due to

the increased amount of Fe(II) centers. S-doped Fe-MOFs might thus become a suitable choice in EF, although the rational design and the involved mechanistic aspects merit deeper investigation [28].

This study constitutes the first attempt to synthesize the ultra-uniform MIL-88B(Fe)/ Fe_3S_4 hybrids via a facile sulfurization, followed by their application in the HEF treatment of trimethoprim (TMP), selected as target pollutant because it is one of the most commonly prescribed antibiotics for the treatment of bacterial infections. TMP has been frequently detected in surface water, municipal sewage and hospital effluents at ng L^{-1} - $\mu\text{g L}^{-1}$ level [29]. The effect of sulfidation conditions on the coordination and physico-chemical properties of the hybrids, as well as on the catalyst activity was systematically evaluated. Then, the influence of critical factors (e.g., initial pH, catalyst dosage and current density), the viability of various micropollutants degradation in urban wastewater and the catalyst reusability in HEF were studied in detail. Finally, the intrinsic mechanism, including the Fe(III)/Fe(II) redox cycling, the role of S species, and the H_2O_2 adsorption and activation is proposed based on the catalyst characterization and density functional theory (DFT) results.

2. Experimental

2.1. Chemicals

Trimethoprim, naproxen, bisphenol A, ciprofloxacin and 2,4-dichlorophenol were purchased from Sigma-Aldrich and Merck. Sodium sulfate, sodium hydroxide pellets and concentrated sulfuric acid were purchased from Merck. $\text{FeCl}_3 \cdot 6\text{H}_2\text{O}$, *p*-phthalic acid (H_2BDC), dimethylformamide (DMF) and thioacetamide (TAA) from Sigma-Aldrich were employed for the synthesis of the MIL-88B(Fe)/ Fe_3S_4 hybrids. Analytical grade TiOSO_4 used for H_2O_2 determination and 1,10-phenanthroline monohydrate needed for determining the leached iron concentration were acquired from Merck. Organic solvents of HPLC grade and all the other chemicals were supplied by Sigma-Aldrich and Merck. The urban wastewater for selected trials was collected from the secondary effluent of a wastewater treatment facility located near Chongqing, being immediately preserved at 4 °C to keep constant its main properties: total organic carbon (TOC) of 4.6 mg C L^{-1} , 15.9 mg L^{-1} COD and 12.5 mg L^{-1} $\text{NH}_4\text{-N}$. In all other cases, the solutions were prepared with water of resistivity greater than 18.2 $\text{M}\Omega \text{ cm}$, obtained from a Millipore Milli-Q system.

2.2. Catalyst synthesis

The route for synthesis of MIL-88B(Fe)/ Fe_3S_4 hybrids is schematized in Fig. 1a. MIL-88B(Fe) was first prepared following a typical solvothermal methodology. $\text{FeCl}_3 \cdot 6\text{H}_2\text{O}$ and H_2BDC (10 mmol of each) were dissolved in 50 mL DMF to form a homogeneous solution. Then, 4 mL of 2 M NaOH solution were added dropwise under vigorous stirring. The as-obtained yellow mixed solution was transferred into a 100 mL Teflon-lined stainless steel autoclave and heated at 100 °C for 12 h. Once cooled down naturally, the resulting powder was collected by centrifugation and repeatedly rinsed with ultrapure water and ethanol. The final MIL-88B(Fe) was dried overnight in a vacuum drying oven at 60 °C.

To prepare the MIL-88B(Fe)/ Fe_3S_4 hybrids, 200 mg MIL-88B(Fe) were suspended in 50 mL ethanol solution, then a certain amount of TAA was added as sulfidation reagent and the mixture was sonicated for 20 min to ensure homogeneity. The solution was sealed in the Teflon-lined autoclave to conduct solvothermal reaction at 150 °C for 3 h. Once cooled down, the final black solid product was collected by centrifugation, washed exhaustively with ultrapure water and ethanol, and dried overnight in a vacuum drying oven at 60 °C. The product was named as S-MIL-88B-3h-x (where x denotes the mass ratio of TAA to MIL-88B(Fe), i.e., 0.5:1, 1:1, 2:1, 3:1 and 4:1). Similarly, the catalysts prepared at different hydrothermal treatment time under the TAA/MIL-88B(Fe) ratio of 3 was named as S-MIL-88B-yh-3 (where y denotes the

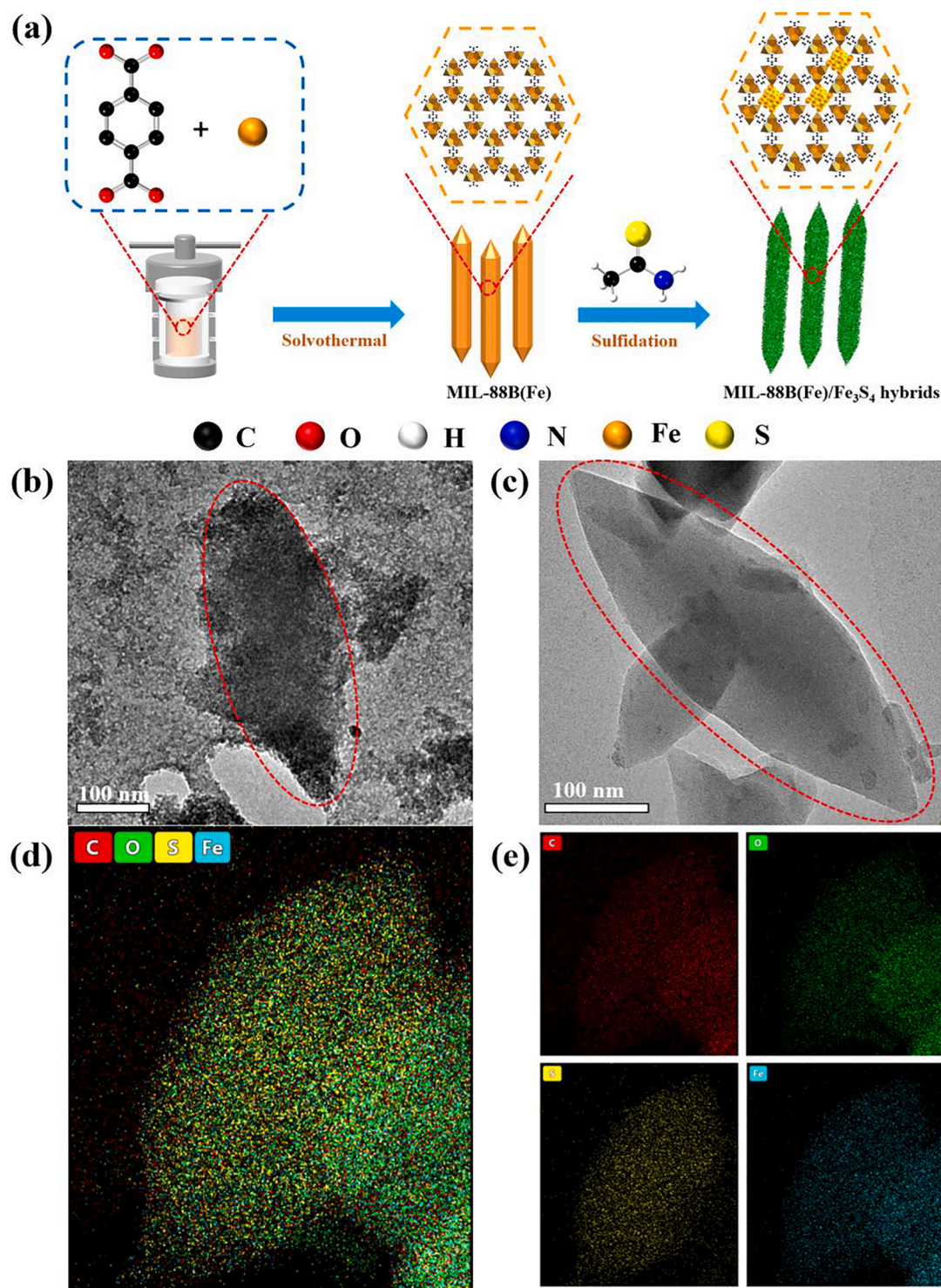


Fig. 1. (a) Scheme of the synthesis route to sulfidation-engineered MIL-88B(Fe)/Fe₃S₄ hybrids. TEM images of (b) MIL-88B(Fe) and (c) S-MIL-88B-3h-3. (d) EDS mapping displaying the uniform dispersion of elements in S-MIL-88B-3h-3.

treatment time, i.e., 1, 2, 3 and 4 h).

2.3. Catalyst characterization

The morphology of the catalyst was observed by high-resolution transmission electron microscopy (HRTEM) using a FEI TF20 microscope that was operated at 200 kV. The microscope was coupled to an energy dispersive X-ray (EDX) detector for mapping acquisition. For X-ray diffraction (XRD) analysis, an X-ray powder diffractometer (Rigaku

SmartLab) was employed, using Cu K α radiation ($\lambda = 1.5406 \text{ \AA}$) and operating at 40 kV and 20 mA. X-ray photoelectron spectroscopy (XPS) measurements for the elucidation of the chemical states were obtained in an ultrahigh vacuum spectrometer equipped with a VSW Class WA hemispherical electron analyzer (Thermo Scientific K-Alpha spectrometer). Fourier transform-infrared (FT-IR) spectra were collected using a Thermo Scientific Nicolet iS20 FTIR spectrometer, at room temperature. The specific surface area of the catalysts was obtained with the Brunauer–Emmett–Teller (BET) analyzer, and the particle size distribution

was determined by dynamic light scattering (DLS) using a Malvern Zetasizer Nano ZS90 laser diffraction particle size analyzer. The magnetization characterization was carried out on a LakeShore7404 vibrating sample magnetometer (VSM). Electrochemical impedance spectroscopy (EIS) and Tafel polarization were performed using a CHI 760E electrochemical workstation. The details are described in Text S1 of [Supplementary Material \(SM\)](#).

The structural modelling and DFT calculations were carried out with the Vienna Ab initio simulation package (VASP). The exchange–correlation interaction was described by generalized gradient approximation of Perdew–Burke–Ernzerhof (GGA–PBE). The projector augmented-wave (PAW) method was employed to treat interactions between ion cores and valence electrons. The plane-wave cut-off energy was fixed to 450 eV. During the relaxation, the Brillouin zone was sampled by $2 \times 2 \times 1$ K-point grid. And the vacuum slab was set up to 20 Å.

2.4. Electrochemical systems and analytical procedures

The electrolytic trials to evaluate the degradation performance were performed in a single-chamber glass cell containing 160 mL of 0.050 M Na_2SO_4 solution and a given concentration of TMP (and other micro-pollutants in some trials), at 25 °C and kept under vigorous magnetic stirring. The anode was a commercial IrO_2 -based plate (i.e., dimensionally stable anode, DSA) in most of the assays, although a boron-doped diamond (BDD) thin film on Si substrate was employed for comparison. The anode had a geometric surface area of 3 cm² (i.e., area exposed to the solution), as was also the case of the cathode made with carbon-polytetrafluoroethylene (PTFE) on carbon cloth. This material was purchased from BASF and placed inside a tubular gas chamber to be fed with atmospheric air pumped at flow rate of 1 L min⁻¹ for H_2O_2 generation. The electrodes were mounted with a gap of 1.0 cm between each other. The EF treatments started after the addition of the catalyst and the supply of a constant current from a DC power source (IT6322A from ITECH, China). For cycling tests, the catalyst was recovered by centrifugation, washed with ultrapure water and dried overnight in a vacuum drying oven at 60 °C.

The pH was measured with a PHS-3C pH-meter. At selected time intervals, samples were collected and filtered (0.2 µm PTFE syringe filters) prior to analysis to remove the solid. The H_2O_2 concentration accumulated during the electrolytic trials was determined from the absorbance of the complex formed between the oxidant and a Ti(IV) reagent, using a UNIC UV2365 UV/Vis spectrophotometer ($\lambda = 408$ nm, 25 °C) [30]. The iron concentration leached from the catalyst was quantified from the absorbance of the complex formed between Fe^{2+} and 1,10-phenanthroline, employing the same spectrophotometer ($\lambda = 510$ nm, 25 °C). Some of these results were also confirmed by means of inductively-coupled plasma optical emission spectrometry (ICP-OES, performed with a ICPS-8100 instrument from Shimadzu). TMP concentration was determined by HPLC using a SCION6000 chromatograph equipped with a CHromcore C18 5 µm (250 mm × 4.6 mm) column, thermostated at 35 °C, and a SC6000 detector set at 270 nm. A mixture of CH_3OH and 0.010 M KH_2PO_4 solution at pH 3.0, with ratio 30:70 (v/v), was eluted at 1.0 mL min⁻¹ as mobile phase, disclosing a well-defined peak corresponding to TMP at retention time of 4.8 min. The TOC concentration was measured with a TOC analyzer (TOC-L CPH, Shimadzu). The S content of catalysts was analyzed by inductively coupled plasma with optical emission spectroscopy (ICP-OES, Agilent 5110). The reaction intermediates were identified by LC-QTOF-MS analysis, which was carried out using a Chromatograph Ultimate 3000 (Thermo Scientific) coupled to an LTQ Orbitrap Velos mass spectrometer (Thermo Scientific), operating in positive ion mode. An Acquity UPLC BEH C18 column 1.7 µm (50 mm × 2.1 mm) column, at 40 °C, was utilized. The chromatograph also had a UV detector, which was set at 270 nm. The mobile phase was a mixture of CH_3CN (A) and 0.1% CH_3COOH (B) eluted at 0.3 mL min⁻¹ according to the following

gradient (t, %B): (0, 5), (15, 50), (16,100), (18,100), (19, 5) and (24, 5).

3. Results and discussion

3.1. Characterization of catalysts

The morphological features of the as-prepared catalysts evaluated by TEM analysis can be observed in [Fig. 1b](#). MIL-88B(Fe) is composed of typical fusiform rods (i.e., spindle-shaped), with length of around 450 nm [17]. After sulfidation, the hybrid S-MIL-88B-3h-3 inherited the morphology and dimensions of its MIL-88B(Fe) precursor ([Fig. 1c](#)), which informs about the good stability of catalyst and the excellent mass transport of species during the synthesis as a result of the strong coordination environment and the high porosity of MIL-88B(Fe). The elemental mapping in [Fig. 1d](#) reveals the outstanding composition uniformity, with C, O, S and Fe elements perfectly distributed in the S-MIL-88B-3h-3, thus discarding the aggregation of Fe_3S_4 particles. The loose backbone of the MIL-88B(Fe) precursor not only prevented the agglomeration of Fe_3S_4 crystals, but it also ensured a wide exposure of active sites that facilitated the electron transfer for reactions during the synthesis [31].

[Fig. 2a](#) depicts the XRD patterns of MIL-88B(Fe) and S-MIL-88B-3h-3. The main peaks for the as-prepared MIL-88B(Fe) appear at 9.1° (002), 10.6° (101), 12.5° (102), 17.7° (200), 21.8° (202), and 26.7° (211), which is in perfect agreement with the simulated diffractogram reported in the CIF database, thus confirming the successful synthesis [31]. These main peaks are present in the pattern of S-MIL-88B-3h-3, being accompanied by characteristic peaks located at 25.4°, 30.0°, 36.3°, 44.9°, 47.8° and 52.4° that can be ascribed to (220), (311), (400), (422), (511) and (440) crystal planes of Fe_3S_4 (JCPDS 16–0713). This proves the co-existence of MIL-88B(Fe) structure and Fe_3S_4 particles after the sulfidation treatment. Worth noting, the position of the diffraction peak corresponding to the (102) facet of MIL-88B(Fe) exhibited a remarkable shift. Such modification of the crystallographic characteristics can be explained by the structural flexibility of MIL-88B(Fe), which induces slight structural changes upon entry of the guest species (i.e., H_2S produced from TAA) into the pore channels [31]. The variations in crystal and pore structures are more clearly evidenced by the N_2 sorption analysis ([Fig. S1a](#), [Fig. S1b](#) and [Table S1](#)). The specific surface area and total pore volume decreased drastically upon sulfidation treatment, which is due to the collapse of pore tunnels and the formation of Fe_3S_4 [32]. However, the DLS analysis in [Fig. S1c](#) reveals a similar particle size distribution in both catalysts, implying that the generated ultra-small Fe_3S_4 crystals are uniformly dispersed on the MIL-88B(Fe) framework, not being detectable by DLS. The diameter of most of the MOF particles was between 400 and 1000 nm, which agrees with the particle size determined by TEM images.

The surface chemical composition and oxidation states of MIL-88B(Fe) and S-MIL-88B-3h-3 were analyzed by XPS. The high resolution Fe 2p spectrum of MIL-88B(Fe) in [Fig. 2b](#) exhibits two sets of fitting peaks, which account for Fe 2p_{2/3} and Fe 2p_{1/2} bands assigned to Fe(III). The peaks centered at 711.08 and 724.79 eV correspond to Fe(III) of Fe–O–C (BDC), whereas those appearing at 713.82 and 729.87 eV are assigned to Fe(III) of μ_3 -OFe [32,33]. In addition, a couple of weaker peaks can be ascribed to Fe(II). These results inform about the predominance of the Fe(III) form of iron species in MIL-88B(Fe). As for S-MIL-88B-3h-3 hybrids, a new peak appearing at 706.43 eV is attributed to the presence of Fe(II)-S species, whereas the peaks at 710.70, 713.41, 724.65 and 728.95 eV corresponded to Fe 2p_{3/2} and Fe 2p_{1/2} of Fe(III), which could be originated from the formation of Fe(III)-S species alongside the presence of the Fe(III) species in MIL-88B(Fe) [34]. Note that significant shifts of the Fe 2p peaks toward lower binding energies can be observed for S-MIL-88B-3h-3, which is attributed to the strong interactions between MIL-88B(Fe) and Fe_3S_4 that affect the electron density of the iron sites [35]. Furthermore, the peak intensities of Fe(II) increased, demonstrating the conversion of Fe(III) into Fe(II) during the

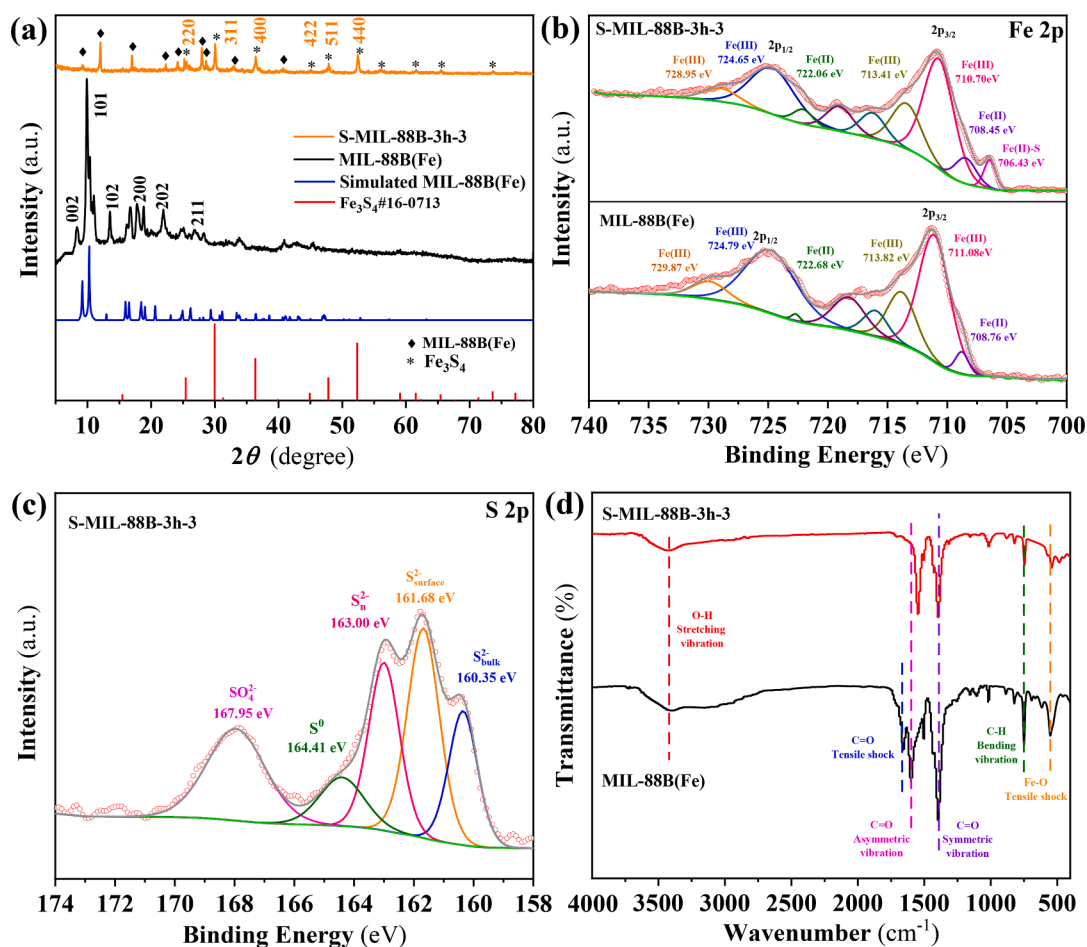


Fig. 2. (a) XRD patterns, (b) Fe 2p XPS spectra, and (d) FTIR spectra of MIL-88B(Fe) and S-MIL-88B-3h-3. (c) S 2p XPS spectrum of S-MIL-88B-3h-3.

sulfidation treatment. The XPS spectrum of S 2p in Fig. 2c has been deconvoluted into five peaks: $\text{S}_{\text{bulk}}^{2-}$, $\text{S}_{\text{surface}}^{2-}$, S_n^{2-} , S^0 and SO_4^{2-} [34,36]. The presence of S_n^{2-} species can be related to the thermodynamically-driven redox process comprising S^{2-} oxidation to S_n^{2-} and Fe(III) reduction to Fe(II) during the sulfidation treatment, which agrees with the increase in the amount of Fe(II) species [37]. The production of S^0 and SO_4^{2-} is attributed to the reactions between S^{2-} and Fe(III) [38,39]. All the possible reactions occurred during the sulfidation are summarized in Table S2. In short, the solvothermal treatment with TAA can modify the chemical and electronic structures of MIL-88B(Fe), generating Fe_3S_4 particles and enhancing the amount of Fe(II) active sites, which are expected to play key roles in H_2O_2 activation. Moreover, the proportion of Fe_3S_4 in S-MIL-88B-3h-3 was determined as 20.8 wt% from the content of S elements measured by ICP-OES/MS (Table S1).

In addition, the FTIR spectra of MIL-88B(Fe) and S-MIL-88B-3h-3 in Fig. 2d inform about the surface functional groups. The peaks at 1657, 1600 and 1393 cm^{-1} for MIL-88B(Fe) are associated to the C=O tensile shock, asymmetric vibration and symmetric vibration of carboxylate groups. The absorption peaks at 3430 and 749 cm^{-1} can be assigned to the O-H stretching vibration and the C-H bending vibration [40]. The characteristic peak at 551 cm^{-1} is related to the Fe-O stretching mode arising from the link between Fe atoms and the ligand. The appearance of these peaks in S-MIL-88B-3h-3 demonstrates the stability of the MIL-88B(Fe). Furthermore, the magnetic properties of S-MIL-88B-3h-3 were verified from the magnetic hysteresis curve, depicted in Fig. S1d. The saturation magnetization (M_s) of S-MIL-88B-3h-3 was 12.7 $\text{emu}\cdot\text{g}^{-1}$, a much higher value than that of MIL-88B(Fe) (2.66 $\text{emu}\cdot\text{g}^{-1}$). The enhanced magnetism upon sulfidation treatment enables the facile post-treatment recovery of the catalyst.

3.2. Evaluation of the catalytic performance

Several systems were applied to treat solutions containing 0.060 mM (i.e., 10 $\text{mg}\cdot\text{C}\cdot\text{L}^{-1}$) TMP + 0.050 M Na_2SO_4 at pH 7.0. Prior to investigate the viability of electrochemical degradation, adsorption trials were carried out. As depicted in Fig. 3a, the presence of either 0.10 $\text{g}\cdot\text{L}^{-1}$ MIL-88B(Fe) or S-MIL-88B-3h-3 as suspended particles in the aforementioned drug solution yielded a TMP removal close to 4%, which means that the contribution of this phenomenon during the following electrochemical trials made at 50 mA can be considered as negligible. The electro-oxidation with electrogenerated H_2O_2 (EO process) in a cell equipped with a DSA plate as the anode allowed achieving a small TMP removal of 22% after 90 min of electrolysis, in agreement with the expected low oxidation power of H_2O_2 and $\text{IrO}_2(\text{OH})$ produced cathodically and anodically, respectively [20]. In contrast, the MIL-88B(Fe)-catalyzed HEF process led to a more substantial degradation of 65% at 90 min, resulting from the formation of $\cdot\text{OH}$ upon occurrence of Fenton's reaction. However, despite possessing a certain ability to trigger the H_2O_2 decomposition, the unsaturated iron active sites of this catalyst were not sufficiently active. In contrast, the S-MIL-88B-3h-3-catalyzed HEF process showed an outstanding performance as compared to all the previous trials, reaching complete TMP abatement in only 45 min. To describe the kinetics of TMP degradation during different electrochemical trials, zero-, first- and second-order models were investigated. As summarized in Table S3, the zero-order model shows the highest correlation coefficients (R^2) for both HEF treatments, indicating that the catalytic reactions agreed with a Langmuir-Hinshelwood mechanism, which means that the active sites on the catalyst surface were substantially covered by TMP and H_2O_2 . In addition, the zero-order kinetic

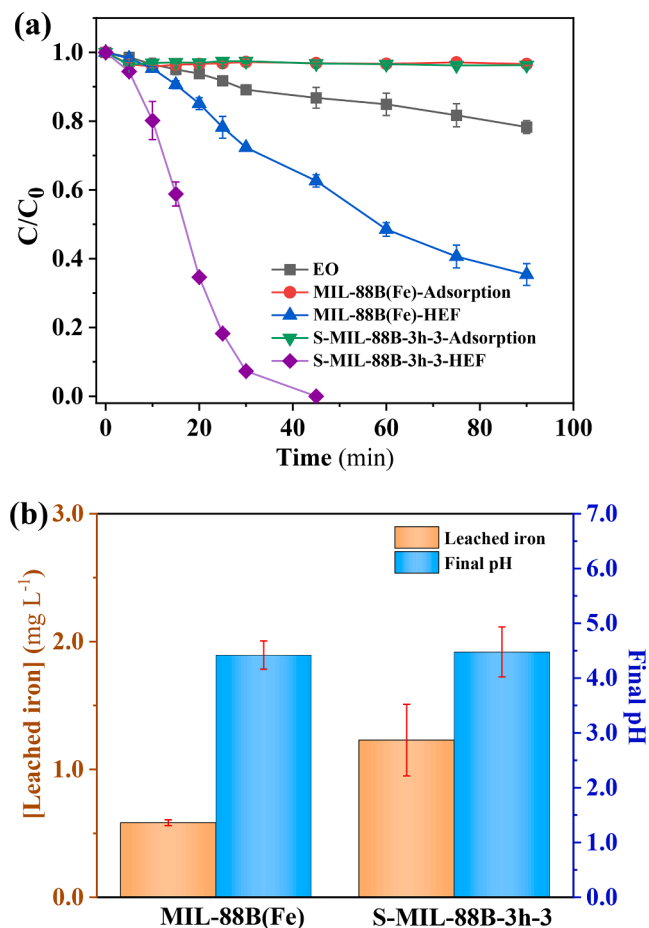


Fig. 3. (a) Normalized TMP decay during the treatment of 160 mL of 0.060 mM drug solutions with 0.05 M Na₂SO₄ under different conditions. General conditions: [Catalyst] = 0.10 g L⁻¹; current = 50 mA; initial pH 7.0; IrO₂-based anode in EO and HEF. (b) Leached iron concentrations and final pH values after 90 min of the trials MIL-88B(Fe)-HEF and S-MIL-88B-3h-3-HEF shown in plot (a).

constant in S-MIL-88B-3h-3-catalyzed EF was 0.3399 mM min⁻¹, being approximately 4-fold greater than that found in HEF with MIL-88B(Fe). In the case of EO, the three models show high *R*² values but, considering that the EO process is usually related to pseudo-first-order kinetics due to the fact that a constant M(OH) amount is produced at the anode surface [11], the *k*-value under such model was determined as 0.0028 min⁻¹. The superior catalytic activity of S-MIL-88B-3h-3 can be assigned to the synergistic effect between MIL-88B(Fe) and Fe₃S₄. The main reactions occurred during the S-MIL-88B-3h-3-catalyzed HEF process are listed in Table S4. The uniformly dispersed Fe(II) species from both MIL-88B(Fe) and Fe₃S₄ act as the active sites for H₂O₂ decomposition to form abundant ·OH. Meanwhile, the S²⁻ and S_n²⁻ species provide electrons for Fe(III) reduction at high rate, continuously renewing the Fe(II) active sites that ensures a fast production of ·OH [37,41]. The unique morphology and structure of the hybrids, namely ultra-small Fe₃S₄ crystals with uniform distribution on/in the MIL-88B(Fe) nanoparticles, ensures the access to plenty of exposed active sites for the catalytic reactions. Fig. 3b evidences a very low iron leaching from both MIL-88B(Fe) and S-MIL-88B-3h-3 during the HEF treatments, being 0.58 and 1.23 mg L⁻¹ at 90 min, respectively, which confirms the great stability of the catalysts. The higher dissolved iron concentration from S-MIL-88B-3h-3 can be due to the partial collapse of the framework during the synthesis and the partial decomposition of Fe₃S₄ during the treatment. In spite of this, the leached Fe concentration is still far below the European Union standard of 2 mg L⁻¹ [42]. Fig. 3b also shows the decrease

of pH in both cases, thanks to the formation of acidic intermediates like carboxylic acids, as well as to the spontaneous acidification occurring upon Fe(III) reduction by S²⁻ to form sulfite or sulfate (Table S4) [14].

The TAA/MIL-88B(Fe) ratio and hydrothermal treatment time are considered crucial factors for the optimization of the sulfidation process, thus being necessary to evaluate the catalytic performance of S-MIL-88B-yh-x in the HEF process. Fig. 4a shows the TMP decays using several S-MIL-88B-3h-x catalysts. The increase in the TAA/MIL-88B(Fe) ratio from 0.5 to 3 gave rise to a substantial promotion in the TMP degradation efficiency, from 50% at 90 min to a faster and total removal. Nonetheless, further increase of the ratio to 4 was detrimental. Note that, at the lowest ratio of 0.5, the sulfidated catalyst exhibited a poorer activity as compared to MIL-88B(Fe), suggesting that such a small amount of TAA causes the collapse of the MIL-88B(Fe) framework but is insufficient to form abundant Fe₃S₄ crystals. This is confirmed by the XRD patterns of the five as-synthesized catalysts (Fig. 4b), where the peak shifts as compared to MIL-88B(Fe) and the absence of Fe₃S₄ peaks are evident for S-MIL-88B-3h-0.5. The progressive increase in the amount of TAA enhanced the structural modification of MIL-88B(Fe) with formation of Fe₃S₄, finding an excellent catalytic performance of the S-MIL-88B-3h-3 catalyst (i.e., ratio of 3) thanks to the optimal Fe₃S₄ content (Fig. 4a). The peaks of MIL-88B(Fe) in S-MIL-88B-3h-4 almost disappeared, implying the severe collapse of the framework with the consequent loss of iron active sites from MIL-88B(Fe). Consequently, the poor mass transport due to that collapse of the porous structure decelerated the TMP degradation. In addition, the iron leaching during the TMP treatment was kept low but it increased sharply at an excessive TAA/MIL-88B(Fe) ratio (Fig. S2a), which informs about the importance of the strong coordination between metal atoms and ligands in MIL-88B(Fe) to stabilize the iron active sites, avoiding their loss during the HEF treatment. The MIL-88B(Fe) owns a topological Fe₃O(BDC)₃ structure, in which Fe atoms exhibit an octahedral environment that is terminated by some nonbridging ligands like water, a unique structure that confers excellent stability to the Fe sites [18].

Once established that a ratio of 3 was optimum, the catalytic performance of S-MIL-88B-yh-3 was investigated. In Fig. 4c, the superiority of the S-MIL-88B-3h-3 sample is corroborated, since the TMP removal efficiency increased as the hydrothermal treatment time was prolonged from 1 to 3 h, whereupon a longer time became detrimental. These results demonstrate again that insufficient sulfidation certainly alters the backbone of MIL-88B(Fe) but yields a small amount of Fe₃S₄, whereas an excessively long synthesis may destroy most of the MIL-88B(Fe) particles, leaving the Fe₃S₄ crystals irregularly distributed on a structurally affected MOF support (Fig. S2c). The highest dissolved iron concentration found using the S-MIL-88B-4h-3 in HEF (Fig. S2b) confirms the crucial role of MIL-88B(Fe) to ensure the catalyst stability.

The effect of initial solution pH, catalyst dosage and applied current on the drug concentration decay when operating the S-MIL-88B-3h-3-catalyzed HEF system is displayed in Fig. 4d-f. As can be observed in Fig. 4d, the fastest TMP decay was achieved at initial pH 3.0, attaining the total removal after only 30 min, which can be ascribed to the greater oxidation potential of ·OH at pH 3.0 and the increased iron solubilization (7.1 mg L⁻¹ at 90 min, Fig. S2d). The latter phenomenon results in a larger ·OH production from homogenous Fenton's reaction (1) [14]. Note that such large accumulation of dissolved iron at initial pH 3.0 implies the intolerance of S-MIL-88B-3h-3 to strong acidic condition. Fortunately, total removal of TMP could be still obtained at 45 min at initial pH 5.0–7.0, whereas TMP concentration decay of 96% at 90 min was attained at initial pH 9.0. The final leached iron content in these trials was lower than 2.0 mg L⁻¹ (Fig. S2d), a very positive finding referred to the stability of S-MIL-88B-3h-3 at mild pH. In contrast, a remarkably poor TMP removal of 22% was observed at initial pH 11.0 due to the relatively low oxidation potential of ·OH and the self-decomposition of H₂O₂ at alkaline pH [18]. Therefore, it can be concluded that the S-MIL-88B-3h-3-catalyzed HEF is advantageous to work over a wide pH range. The solutions became acidified in all cases

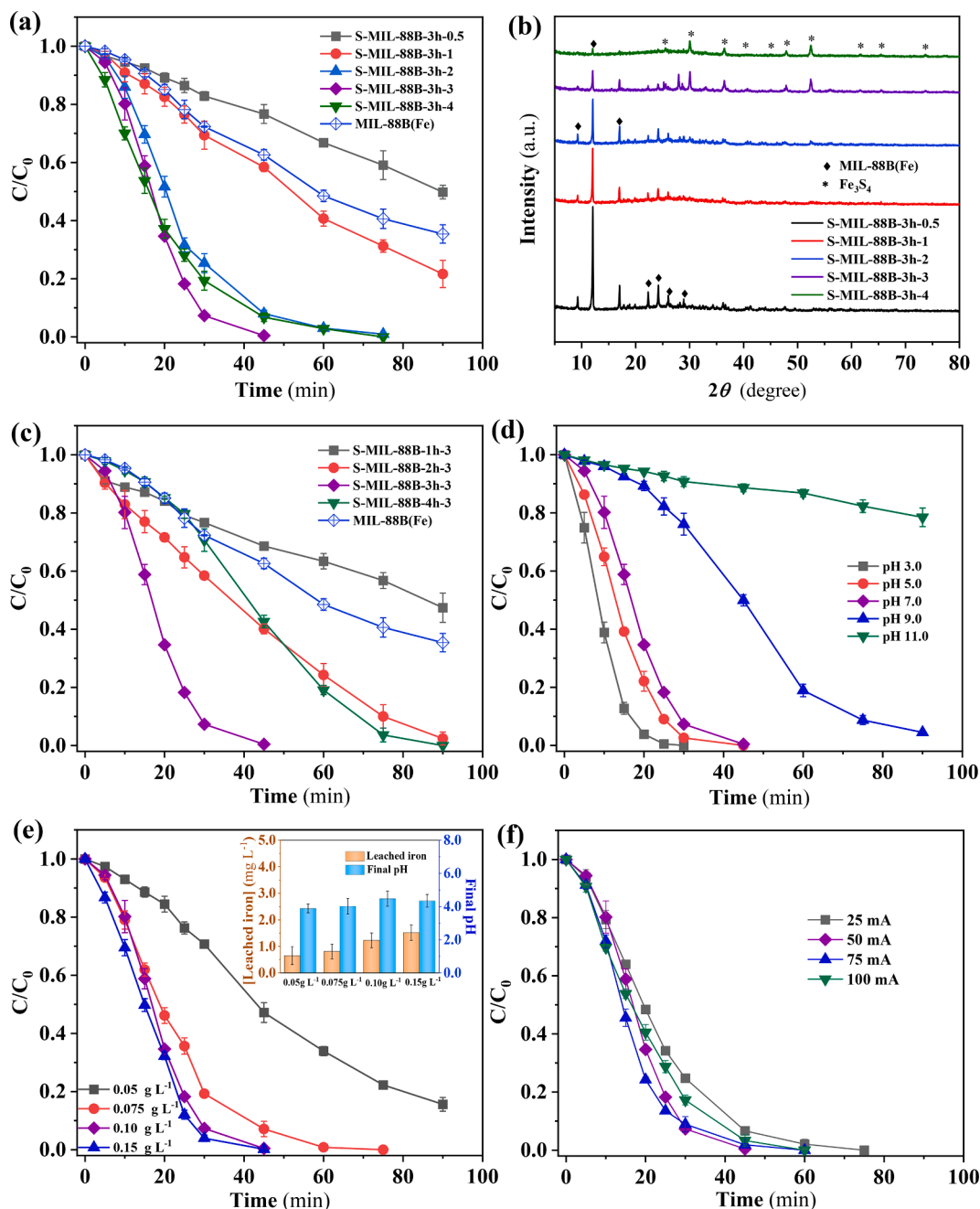


Fig. 4. (a) Effect of TAA/MIL-88B(Fe) ratio (employed for the catalyst synthesis) on the HEF performance and (b) XRD pattern for each catalyst. (c) Effect of hydrothermal treatment time (employed for the catalyst synthesis) on the HEF performance. Effects of (d) initial pH, (e) catalyst dosage and (f) applied current on TMP decay in the S-MIL-88B-3h-3-catalyzed HEF system. The inset in plot (e) shows the leached iron concentrations and final pH values after 90 min of the trials depicted in the main plot. General conditions, except when a specific parameter is modified: $[TMP]_0 = 0.060$ mM (+0.050 M Na_2SO_4); [catalyst] = 0.10 g L⁻¹; current = 50 mA; initial pH 7.0; IrO_2 -based anode.

(Fig. S2d), owing to the production of acidic organic by-products and pH self-regulation (Table S4) [14].

Fig. 4e highlights that a higher amount of catalyst from 0.05 to 0.10 g L⁻¹ gives rise to a substantial enhancement in the TMP degradation efficiency, increasing from 53% to >98% at 45 min. The increase in the catalyst dosage provides more available active sites for the H_2O_2 adsorption and activation, generating abundant $\cdot OH$ to destroy TMP. Conversely, when increasing to 0.15 g L⁻¹, the acceleration of the degradation was insignificant, probably due to the parasitic reaction between excessive iron sites and $\cdot OH$ [10]. Moreover, at the greatest catalyst content, a more severe iron leaching was found (insert figure), thereby confirming that the optimum dosage was 0.10 g L⁻¹.

As can be seen in Fig. 4f, the applied current played a minor role in the S-MIL-88B-3h-3-catalyzed HEF, since quite similar TMP decays were obtained (i.e., 94%, 97%, 98% and 100% at 45 min, respectively). Fig. S2e depicts the H_2O_2 concentration accumulation in the solution from reaction (3), gradually rising at higher applied current. However, this improvement was not realized in a considerably faster TMP removal, suggesting that an excess of H_2O_2 is mostly wasted because the rate of heterogeneous Fenton's reaction is actually limited by the availability and activity of the given catalyst. Instead, a further rise in current to 100 mA was detrimental due to the scavenging reaction occurring between $\cdot OH$ and the excess of accumulated H_2O_2 [10,31].

3.3. Recyclability of the catalyst and treatment of micropollutants in urban wastewater

The reusability of Fenton catalysts is one of the critical issues to be addressed for practical application of this type of EAOPs. The evaluation was conducted upon simple magnetic recovery of the S-MIL-88B-3h-3 catalyst from the treated solution, followed by washing with ultrapure water. Note that the recovery percentage of the catalyst reached up to $95 \pm 3\%$. As illustrated in Fig. 5a, the TMP concentration diminished completely in 45 min in the first three runs, whereas it was still possible to achieve more than 90% TMP removal in the 4th cycle. These results demonstrate the relatively high reusability of the catalyst for HEF. The

slower degradation once a certain number of cycles has been performed can be accounted for by surface passivation and deactivation, as well as by the spontaneous acidification during the runs that contributes to some iron leaching. Therefore, the used catalyst after the fourth trial was characterized by XRD and XPS, trying to correlate the observed behavior with the chemical and structural changes. The XRD patterns in Fig. S3, corresponding to fresh and used S-MIL-88B-3h-3, demonstrated that the crystallinity of the catalyst remained quite stable along the treatment, without any obvious alteration. The Fe 2p spectra depicted in Fig. 5b highlight the significant reduction of the peak intensities of Fe(II)-S and other Fe(II) species, implying the intense consumption of Fe(II) active sites by Fenton's reaction during the four consecutive cycles. Regarding

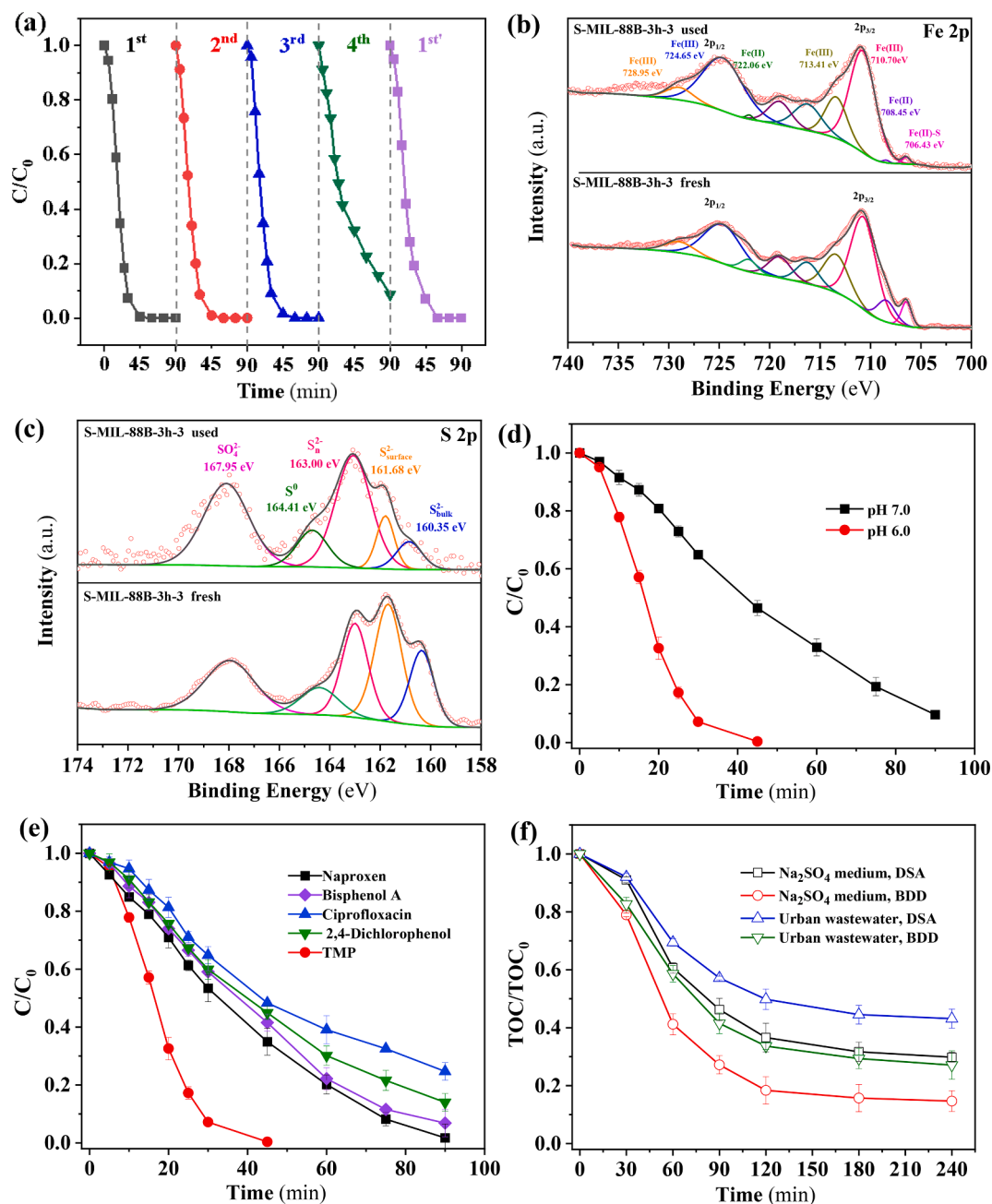


Fig. 5. (a) Reusability of S-MIL-88B-3h-3 catalyst in four consecutive 90-min HEF runs with 0.10 mg L^{-1} catalyst under the conditions described in Fig. 3a. Cycle 1st was made once the catalyst regeneration was performed at the end of the fourth cycle. (b) Fe 2p and (c) S 2p XPS spectra of fresh and used S-MIL-88B-3h-3 catalyst. (d) Treatment of TMP spiked into urban wastewater by S-MIL-88B-3h-3-catalyzed HEF at initial pH 6.0 and 7.0. (e) Normalized decay of micropollutants concentration during the HEF treatment of 160 mL of solutions containing one of the contaminants (at 10 mg C L^{-1}) spiked into urban wastewater at initial pH 6.0. (f) TOC abatement during the HEF treatment of 0.060 mM TMP solutions (using 0.050 M Na₂SO₄ or urban wastewater) with a DSA or BDD anode. General conditions, except when a specific parameter is modified: [TMP]₀ = 0.060 mM; [catalyst] = 0.10 g L^{-1} ; current = 50 mA; initial pH 7.0; IrO₂-based anode.

to S 2p spectra in Fig. 5c, the decrease in the peak intensities of S_{bulk}^{2-} and S_{surface}^{2-} species and the increase in those of S_{Fe}^{2-} , S^0 and SO_4^{2-} species when comparing the fresh and used catalyst is a clear proof of the promotion of reactions listed in Table S4 by S^{2-} . The electrons are transferred from the S_{bulk}^{2-} and S_{surface}^{2-} species to the Fe(III) sites during the catalysis, leading to the Fe(III)-to-Fe(II) conversion and the formation of oxidized sulfur species [41]. Hence, the progressive consumption of S^{2-} species at the catalyst surface decelerates the Fe(II) regeneration, eventually reducing the production of $\cdot\text{OH}$ for TMP degradation. Despite the inevitable deactivation of the catalyst, proper cleaning with methanol and 10 mM HCl allowed its complete regeneration, being feasible to recover 100% TMP decay in 60 min (cycle 1st in Fig. 5a). This was due to the fact that the loss of S^{2-} species pre-eminently occurs at the surface of the catalyst and thus, the generated sulfur species (S^0 and SO_4^{2-}) can be removed by facile washing with methanol [34]. As another interesting feature to support the good stability, note that the dissolved iron concentration from S-MIL-88B-3h-3 was much lower than that from relatively pure Fe_3S_4 (Fig. S2a and S2b), which also implied the suppressed decomposition of Fe_3S_4 in S-MIL-88B-3h-3 due to the unique structure of MIL-88B (Fe).

The high performance of S-MIL-88B-3h-3 catalyzed HEF treatment of several micropollutants spiked into urban wastewater was further confirmed (Fig. 5d and e). It is highlighted that 90% TMP could be removed at initial pH 7.0, a worse behavior than that observed in 0.050 M Na_2SO_4 medium (Fig. 3a) due to the role of inorganic carbon and natural organic matter as $\cdot\text{OH}$ scavengers, but still quite effective. Worth noting, the decay of TMP concentration was complete at 45 min at a slightly more acidic pH of 6.0 (Fig. 5d), which can be attributed to the partial removal of inorganic carbon and increased catalytic activity. Moreover, the HEF treatment of other four ubiquitous micropollutants like naproxen, bisphenol A, ciprofloxacin and 2,4-dichlorophenol spiked into urban wastewater at pH 6.0 was evaluated positively, as shown in Fig. 5e. The treatment was very efficient for the former two, attaining 100% and 94%, respectively, at 90 min, whereas 86% disappearance of 2,4-dichlorophenol and 76% destruction of ciprofloxacin were achieved. The difference in their degradation kinetics can be related to the specific structure of the target molecules, which affects their interaction and reactivity with $\cdot\text{OH}$. Finally, the performance of the S-MIL-88B-3h-3-catalyzed HEF treatment was not only evaluated by determining the time course of the TMP concentration but also by assessing the trend of solution TOC in both sulfate medium and urban wastewater. Fig. 5f reveals substantial TOC abatements of 70% and 57% in sulfate and

wastewater, respectively, after 240 min of treatment employing the IrO_2 -based DSA anode at 50 mA. When replacing the anode by BDD, the TOC abatement was significantly increased to 86% and 73% at 240 min, which is attributed to the production of a much stronger oxidant like physisorbed $\text{BDD}(\cdot\text{OH})$ [43]. This is not as free in solution as the $\cdot\text{OH}$ produced via Fenton's reaction, but it is clearly superior to $\text{IrO}_2(\cdot\text{OH})$. On the other hand, the presence of natural organic matter retarded the TOC abatement in urban wastewater. Note that a very negligible TOC decay could be achieved during the last 120 min treatment in all the cases, probably because of the accumulation of small persistent but non-toxic (i.e., non-aromatic) organic molecules.

3.4. Identification of aromatic intermediates and proposed TMP degradation routes

As summarized in Table S5, six main aromatic intermediates generated during the TMP degradation were identified by LC-QTOF-MS analysis. The prevailing degradation routes were thus proposed (Fig. 6), involving carbonylation, consecutive pure hydroxylation and mixed hydroxylation steps accompanied either by oxidation or loss of methoxy group. The direct attack of TMP by $\cdot\text{OH}$ and $\text{M}(\cdot\text{OH})$ may cause carbonylation at the methylene bridge, giving rise to the primary product **P1** [44]. Hydroxylation in one of the methoxy positions of the benzene ring was confirmed by the production of intermediate **P2**, also reported by other authors [45]. Hydroxylation has been widely reported as the preferred pathway in other AOPs [46,47]; hydrogen abstraction of the bridge $-\text{CH}_2-$ group by $\cdot\text{OH}$ resulted in the formation of a carbon-centered radical, which was followed by the reaction with molecular oxygen and elimination of the hydroperoxyl radical, finally yielding the α -hydroxytrimethoprim product **P3**. Further oxidation of **P3** also gave rise to the keto-derivative **P1**. Note that the addition of electrophilic $\cdot\text{OH}$ to the aromatic ring of TMP agreed with the same hydrogen abstraction mechanism, originating the monohydroxylated by-product **P4**. Moreover, the latter underwent subsequent $\cdot\text{OH}$ attack, leading to the formation of di- (**P5**) and tetra- (**P6**) hydroxylated compounds via the hydroxylation reactions, being accompanied by the loss of all methoxy groups in the case of **P6** generation. Alternatively, the hydroxylation of **P2** can also justify the production of **P6**. Note that the loss of N atoms in N-containing compounds like TMP can give rise to inorganic ions such as NH_4^+ , NO_3^- and NO_2^- [48]. As reported elsewhere, it is expected that 20–40% of initial N is transformed into NH_4^+ and NO_3^- , without no trace of NO_2^- , during Fenton-based treatments [44,49].

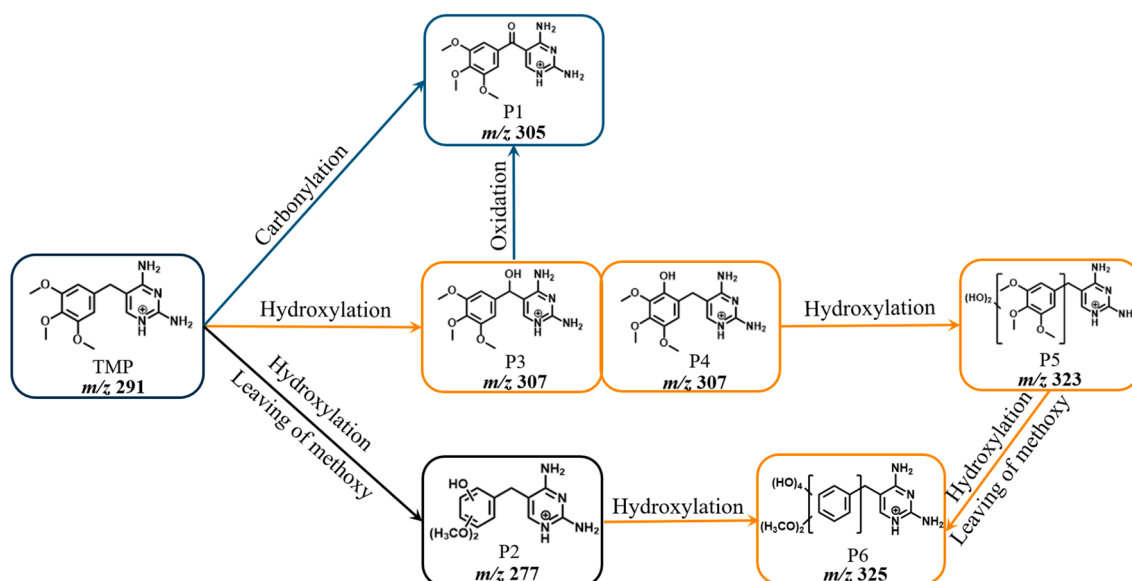


Fig. 6. Proposed routes for the degradation of TMP by S-MIL-88B-3h-3-catalyzed HEF treatment at neutral pH.

3.5. Mechanistic insights

EIS and Tafel tests were first carried out to investigate the electron transfer capability of the catalysts. The Nyquist plots of S-MIL-88B-3h-3 and MIL-88B(Fe) samples are displayed in Fig. S4a, with the equivalent circuit shown inside. The interfacial charge-transfer resistance (R_{ct}) obtained from the semicircle arcs reflects the electron transfer capability [50]. The R_{ct} value of S-MIL-88B-3h-3 (1.1 k Ω) was much lower than that of MIL-88B(Fe) (7.6 k Ω), implying a much faster charge transfer kinetics using the S-MIL-88B-3h-3. On the other hand, the Tafel slopes for the polarization curves obtained with both samples are compared in Fig. S4b, being 66 and 83 mV dec⁻¹ using S-MIL-88B-3h-3 and MIL-88B(Fe) catalyst, respectively. Since a lower Tafel slope can be correlated with a greater catalytic activity, it is evident that the S-MIL-88B-3h-3 catalyst possess a faster electron transfer rate, requiring a lower overpotential to reach a given current [51]. These results agree with the R_{ct} values from the EIS test. The higher electron transfer efficiency of S-MIL-88B-3h-3 can thus contribute to accelerate the activation of H₂O₂ and the Fe(III)-to-Fe(II) conversion, justifying the better catalytic performance in HEF.

To gain a deeper insight into the synergistic effect of MIL-88B(Fe)/Fe₃S₄ hybrids that causes the enhancement of HEF process, the structure modeling, charge density difference and adsorption of H₂O₂ were established by DFT calculations. As shown in Fig. 7a–c, the optimized configurations of MIL-88B(Fe), Fe₃S₄ and their hybrids were successfully constructed through the JCPDS card No. 16–0713 of MIL-88B(Fe) and (400) planes of Fe₃S₄ [52]. The charge density difference was calculated to evaluate the charge transfer and separation at the interface of the hybrids. In Fig. 7d–g, the purple regions denote charge depletion and the azure regions denote charge accumulation. The side and top views of the charge density difference in MIL-88B(Fe) (Fig. 7d and f) reveal that the charge accumulation mainly occurs around the iron atoms, whereas charge depletion is concentrated near the oxygen atom. The facile electron transfer from oxygen to iron could promote the Fe(III)-to-Fe(II) conversion. Regarding to MIL-88B(Fe)/Fe₃S₄ heterostructure, more dense charge accumulation is centered around the iron sites due to

the presence of sulfur atoms (Fig. 7e and 7g). The enhanced charge redistribution is expected to produce more electron-rich iron active sites, and the Fe(III)/Fe(II) redox cycling could be accelerated by promoting the electron transfer speed [53]. The adsorption energy (E_{ads}) of H₂O₂ on the catalysts was calculated by the following equation to further evaluate the catalytic performance:

$$E_{ads} = E_{total} - E_{H_2O_2} - E_{catalyst} \quad (7)$$

where E_{total} is the total energy of H₂O₂/catalyst complexes, and $E_{H_2O_2}$ and $E_{catalyst}$ are the energies of isolated H₂O₂ molecule and catalyst, respectively. As depicted in Fig. 7h and i, the E_{ads} value of MIL-88B(Fe)/Fe₃S₄ hybrids with H₂O₂ (-0.80 eV) is higher (in absolute value) than that using pure MIL-88B(Fe) (-0.63 eV). The negative value of E_{ads} implies the stable adsorption of H₂O₂ on the catalysts, and the more negative binding energy means the stronger interaction between H₂O₂ and MIL-88B(Fe)/Fe₃S₄ hybrids [54]. The DFT results unambiguously reveal the critical role of Fe₃S₄ on the modulation of the electronic structure of the MOF precursor and the enhancement of the catalytic performance during HEF treatments.

Taking into account the aforementioned findings, a thorough catalytic mechanism is proposed in Fig. 8 for the S-MIL-88B-3h-3-catalyzed HEF treatment of TMP at neutral pH. H₂O₂ is first generated at the cathode through 2-electron oxygen reduction reaction (3), thereby being transported to get adsorbed onto the S-MIL-88B-3h-3 particles. The adsorbed H₂O₂ molecules are quickly activated by the Fe(II) active sites from either MIL-88B(Fe) or Fe₃S₄ to form abundant [•]OH, which is responsible for the efficient destruction of TMP molecules. In addition, the M([•]OH) produced via the anodic reaction can also contribute to the degradation. More importantly, the excellent catalytic performance of S-MIL-88B-3h-3 is ensured by the presence of abundant exposed Fe(II) active sites, the acceleration of Fe(III)/Fe(II) redox cycling and the facile mass transport of H₂O₂ to the catalyst. The introduction of well distributed S²⁻ species as electron donors for Fe(III) reduction makes reaction (5) no longer the rate-limiting step of HEF process, as the regeneration of Fe(II) active centers is greatly boosted. Moreover, the partial inheritance of the morphology and crystal structure of MIL-88B

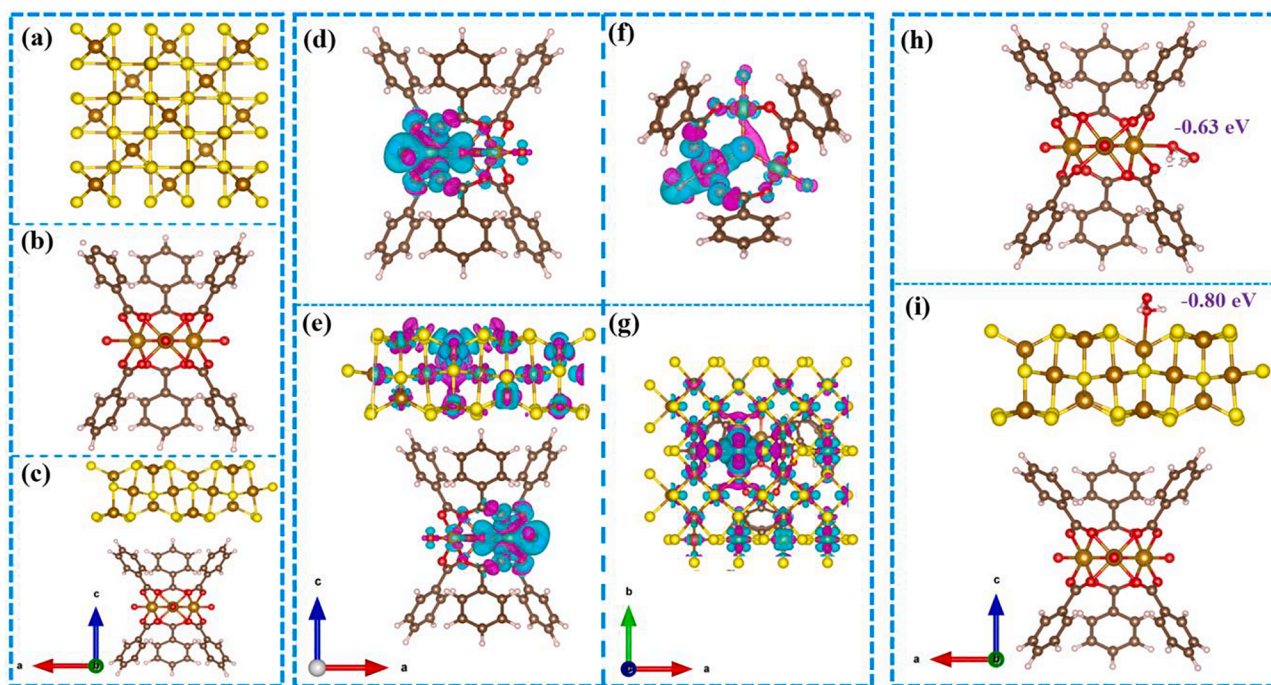


Fig. 7. Optimized structure models of (a) Fe₃S₄, (b) MIL-88B(Fe), and (c) S-MIL-88B-3h-3. (d, e) Side and (f, g) top views of the charge density difference in (d, f) MIL-88B(Fe) and (e, g) S-MIL-88B-3h-3 (The purple regions denote charge depletion while azure regions denote charge accumulation). Side views for H₂O₂ adsorption on (h) MIL-88B(Fe) and (i) S-MIL-88B-3h-3. Color key: C (brown), O (red), H (white), Fe (orange), S (yellow).

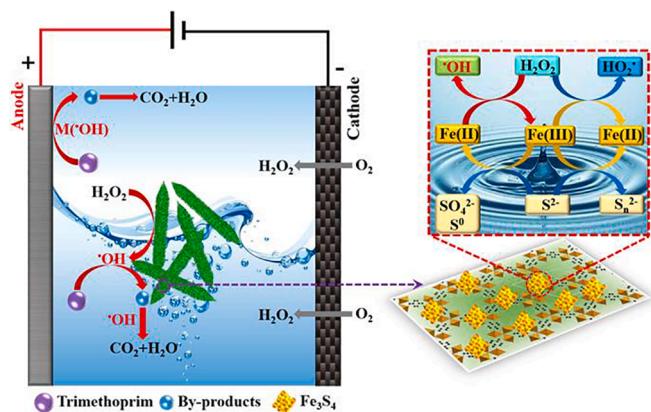


Fig. 8. Proposed mechanism for the S-MIL-88B-3h-3-catalyzed degradation of TMP by HEF treatment at mild pH.

(Fe) precursor largely enhances the stability and recyclability of S-MIL-88B-3h-3 during the treatment.

4. Conclusions

This work proves how rational design results in very effective and stable HEF catalysts to treat micropollutants in actual wastewater. A facile sulfidation strategy to prepare ultra-uniform MIL-88B(Fe)/Fe₃S₄ hybrids as an efficient catalyst in HEF treatment of TMP has been developed. The as-synthesized material owns stable morphological and crystal structure inherited from the MIL-88B(Fe) precursor, allowing the immobilization of ultra-small Fe₃S₄ particles. As a result, the S-MIL-88B-3h-3-catalyzed HEF system achieved the quickest complete removal of TMP at mild pH, only requiring 45 min. A mechanistic study has revealed that the excellent catalytic performance can be attributed to: (i) the acceleration of the Fe(III)/Fe(II) redox cycling by S²⁻ species; (ii) the presence of a higher amount of Fe(II) active centers; (iii) the promotion of the electron transfer rate; and (iv) the efficient mass transport of H₂O₂ towards the catalyst surface. The sulfidation conditions as well as the HEF parameters have been optimized, concluding that the treatment is viable at low catalyst dosage and current over a wide pH range. The S-MIL-88B-3h-3 catalyst undergoes a slight deactivation due to the consumption of S²⁻ species, although reactivation is feasible upon removal of adsorbed sulfur products and organic byproducts by proper rinsing. It can be concluded that sulfidation of MIL-88B(Fe) allows enhancing the catalyst activity at the expense of its stability to a small extent, being these two features identified as the preeminent advantage and disadvantage, respectively. A thorough reaction mechanism for MIL-88B(Fe)/Fe₃S₄-catalyzed HEF treatment of TMP has been finally proposed, opening a new chapter in the practical application of HEF process.

Declaration of Competing Interest

The authors declare that they have no known competing financial interests or personal relationships that could have appeared to influence the work reported in this paper.

Data availability

Data will be made available on request.

Acknowledgements

Funding from the National Natural Science Foundation of China (No. 52100073 and U20A20326), the PhD Gateway Program of Chongqing (CSTB2022BSXM-JCX0140), the Fundamental Research Funds for the Central Universities (2021CDJQY-054, China), and project PID2019-

109291RB-I00 (MCIN/AEI/10.13039/501100011033, Spain) is kindly acknowledged. L.Z. is thankful to his PhD scholarship (State Scholarship Fund, CSC, China).

Appendix A. Supplementary data

Supplementary data to this article can be found online at <https://doi.org/10.1016/j.cej.2022.140757>.

References

- [1] E. Brillas, Progress of homogeneous and heterogeneous electro-Fenton treatments of antibiotics in synthetic and real wastewaters, a critical review on the period 2017–2021, *Sci. Total Environ.* 819 (2022), 153102.
- [2] S.O. Ganiyu, C.A. Martínez-Huitle, M.A. Oturan, Electrochemical advanced oxidation processes for wastewater treatment: advances in formation and detection of reactive species and mechanisms, *Curr. Opin. Electrochem.* 27 (2021), 100678.
- [3] Y. Zhang, G. Daniel, S. Lanzalaco, A.A. Isse, A. Facchin, A. Wang, E. Brillas, C. Durante, I. Sirés, H₂O₂ production at gas-diffusion cathodes made from agarose-derived carbons with different textural properties for acetubolol degradation in chloride media, *J. Hazard. Mater.* 423 (2022), 127005.
- [4] I. Sirés, E. Brillas, Upgrading and expanding the electro-Fenton and related processes, *Curr. Opin. Electrochem.* 27 (2021), 100686.
- [5] G. Daniel, Y. Zhang, S. Lanzalaco, F. Brombin, T. Kosmala, G. Granozzi, A. Wang, E. Brillas, I. Sirés, C. Durante, Chitosan-derived nitrogen-doped carbon electrocatalyst for a sustainable upgrade of oxygen reduction to hydrogen peroxide in UV-assisted electro-Fenton water treatment, *ACS Sustain. Chem. Eng.* 8 (38) (2020) 14425–14440.
- [6] K. Shi, Y. Wang, A. Xu, X. Zhou, H. Zhu, K. Wei, X. Liu, J. Shen, W. Han, Efficient degradation of ibuprofen by electro-Fenton with microtubular gas-diffusion electrodes synthesized by wet-spinning method, *J. Electroanal. Chem.* 897 (2021), 115615.
- [7] N. Barhoumi, N. Oturan, H. Olvera-Vargas, E. Brillas, A. Gadri, S. Ammar, M. A. Oturan, Pyrite as a sustainable catalyst in electro-fenton process for improving oxidation of sulfamethazine. kinetics, mechanism and toxicity assessment, *Water Res.* 94 (2016) 52–61.
- [8] Z. Ye, E. Brillas, F. Centellas, P.L. Cabot, I. Sirés, Electro-Fenton process at mild pH using Fe(III)-EDDS as soluble catalyst and carbon felt as cathode, *Appl. Catal. B: Environ.* 257 (2019), 117907.
- [9] S.D. Sklari, K.V. Plakas, P.N. Petsi, V.T. Zaspalis, A.J. Karabelas, Toward the development of a novel electro-Fenton system for eliminating toxic organic substances from water. Part 2. Preparation, characterization, and evaluation of iron-impregnated carbon felts as cathodic electrodes, *Ind. Eng. Chem. Res.* 54 (7) (2015) 2059–2073.
- [10] Z. Ye, J.A. Padilla, E. Xuriguera, J.L. Beltran, F. Alcaide, E. Brillas, I. Sirés, A highly stable metal-organic framework-engineered Fe₂/C nanocatalyst for heterogeneous electro-Fenton treatment: validation in wastewater at mild pH, *Environ. Sci. Technol.* 54 (2020) 4664–4674.
- [11] E. Brillas, I. Sirés, M.A. Oturan, Electro-Fenton process and related electrochemical technologies based on Fenton's reaction chemistry, *Chem. Rev.* 109 (12) (2009) 6570–6631.
- [12] M. Liu, Z. Feng, X. Luan, W. Chu, H. Zhao, G. Zhao, Accelerated Fe²⁺ regeneration in an effective electro-Fenton process by boosting internal electron transfer to a nitrogen-conjugated Fe(III) complex, *Environ. Sci. Technol.* 55 (9) (2021) 6042–6051.
- [13] T. Yang, D. Yu, D. Wang, T. Yang, Z. Li, M. Wu, M. Petru, J. Crittenden, Accelerating Fe(III)/Fe(II) cycle via Fe(II) substitution for enhancing Fenton-like performance of Fe-MOFs, *Appl. Catal. B: Environ.* 286 (2021), 119859.
- [14] Z. Ye, G.E.M. Schukraft, A. L'Hermitte, Y. Xiong, E. Brillas, C. Petit, I. Sirés, Mechanism and stability of an Fe-based 2D MOF during the photoelectro-Fenton treatment of organic micropollutants under UVA and visible light irradiation, *Water Res.* 184 (2020), 115986.
- [15] P. Dong, H. Wang, W. Liu, S. Wang, Y. Wang, J. Zhang, F. Lin, Y. Wang, C. Zhao, X. Duan, S. Wang, H. Sun, Quasi-MOF derivative-based electrode for efficient electro-Fenton oxidation, *J. Hazard. Mater.* 401 (2021), 123423.
- [16] T. Hu, L. Tang, H. Feng, J. Zhang, X. Li, Y. Zou, Z. Lu, W. Tang, Metal-organic frameworks (MOFs) and their derivatives as emerging catalysts for electro-Fenton process in water purification, *Coord. Chem. Rev.* 451 (2022), 214277.
- [17] Z. Ye, J.A. Padilla, E. Xuriguera, E. Brillas, I. Sirés, Magnetic MIL(Fe)-type MOF-derived N-doped nano-ZVI@C rods as heterogeneous catalyst for the electro-Fenton degradation of gemfibrozil in a complex aqueous matrix, *Appl. Catal. B: Environ.* 266 (2020), 118604.
- [18] C. Gao, S. Chen, X. Quan, H. Yu, Y. Zhang, Enhanced Fenton-like catalysis by iron-based metal organic frameworks for degradation of organic pollutants, *J. Catal.* 356 (2017) (2017) 125–132.
- [19] M. Ahmad, X. Quan, S. Chen, H. Yu, Tuning Lewis acidity of MIL-88B-Fe with mix-valence coordinatively unsaturated iron centers on ultrathin Ti₃C₂ nanosheets for efficient photo-Fenton reaction, *Appl. Catal. B: Environ.* 264 (2020), 118534.
- [20] Z. Ye, R. Oriol, C. Yang, I. Sirés, X. Li, A novel NH₂-MIL-88B(Fe)-modified ceramic membrane for the integration of electro-Fenton and filtration processes: a case study on naproxen degradation, *Chem. Eng. J.* 433 (2022), 133547.

- [21] C. Gao, Y. Su, X. Quan, V.K. Sharma, S. Chen, H. Yu, Y. Zhang, J. Niu, Electronic modulation of iron-bearing heterogeneous catalysts to accelerate Fe(III)/Fe(II) redox cycle for highly efficient Fenton-like catalysis, *Appl. Catal. B: Environ.* 276 (2020), 119016.
- [22] C. Lai, X. Shi, L. Li, M. Cheng, X. Liu, S. Liu, B. Li, H. Yi, L. Qin, M. Zhang, N. An, Enhancing iron redox cycling for promoting heterogeneous Fenton performance: a review, *Sci. Total Environ.* 775 (2021) 145850.
- [23] Q. Wu, H. Yang, L. Kang, Z. Gao, F. Ren, Fe-based metal-organic frameworks as Fenton-like catalysts for highly efficient degradation of tetracycline hydrochloride over a wide pH range: acceleration of Fe(II)/Fe(III) cycle under visible light irradiation, *Appl. Catal. B: Environ.* 263 (2020), 118282.
- [24] J. Tang, J. Wang, Iron-copper bimetallic metal-organic frameworks for efficient Fenton-like degradation of sulfamethoxazole under mild conditions, *Chemosphere* 241 (2020), 125002.
- [25] X. Tian, T. Luo, Y. Nie, J. Shi, Y. Tian, D.D. Dionysiou, Y. Wang, New insight into a Fenton-like reaction mechanism over sulfidated β -FeOOH: key role of sulfidation in efficient iron(III) reduction and sulfate radical generation, *Environ. Sci. Technol.* 56 (9) (2022) 5542–5551.
- [26] N. Barhoumi, L. Labiadh, M.A. Oturan, N. Oturan, A. Gadri, S. Ammar, E. Brillas, Electrochemical mineralization of the antibiotic levofloxacin by electro-Fenton-pyrite process, *Chemosphere* 141 (2015) 250–257.
- [27] J. Hang, X.H. Yi, C.C. Wang, H.F. Fu, P. Wang, Y.J. Zhao, Heterogeneous photo-Fenton degradation toward sulfonamide matrix over magnetic Fe₃S₄ derived from MIL-100(Fe), *J. Hazard. Mater.* 424 (2022), 127415.
- [28] X. Du, W. Fu, P. Su, Q. Zhang, M. Zhou, S-doped MIL-53 as efficient heterogeneous electro-Fenton catalyst for degradation of sulfamethazine at circumneutral pH, *J. Hazard. Mater.* 424 (2022), 127674.
- [29] S. Wang, J. Wang, Trimethoprim degradation by Fenton and Fe(II)-activated persulfate processes, *Chemosphere* 191 (2018) 97–105.
- [30] F.J. Welcher, *Standard Methods of Chemical Analysis*, vol. 2 (1975) sixth ed., R.E. Krieger Publishing Co, Huntington, New York, Part B.
- [31] S. Zhang, Y. Zhuo, C.I. Ezugwu, C.-C. Wang, C. Li, S. Liu, Synergetic molecular oxygen activation and catalytic oxidation of formaldehyde over defective MIL-88B(Fe) nanorods at room temperature, *Environ. Sci. Technol.* 55 (12) (2021) 8341–8350.
- [32] Z.-D. Lei, Y.-C. Xue, W.-Q. Chen, L. Li, W.-H. Qiu, Y. Zhang, L. Tang, The influence of carbon nitride nanosheets doping on the crystalline formation of MIL-88B(Fe) and the photocatalytic activities, *Small* 14 (35) (2018) e1802045.
- [33] H. Zhang, X. Gong, Z. Song, S. Zhang, W. Du, T.T. Nguyen, M. Guo, X. Gao, Wood-based carbon quantum dots for enhanced photocatalysis of MIL-88B(Fe), *Opt. Mater.* 113 (2021), 110865.
- [34] Y. Shi, X. Wang, X. Liu, C. Ling, W. Shen, L. Zhang, Visible light promoted Fe₃S₄ Fenton oxidation of atrazine, *Appl. Catal. B: Environ.* 277 (2020), 119229.
- [35] M. Kaur, S.K. Mehta, P. Devi, S.K. Kansal, Bi₂WO₆/NH₂-MIL-88B(Fe) heterostructure: an efficient sunlight driven photocatalyst for the degradation of antibiotic tetracycline in aqueous medium, *Adv. Powder Technol.* 32 (2021) 4788–4804.
- [36] H. Wu, J. Liu, H. Liang, D. Zang, Sandwich-like Fe₃O₄/Fe₃S₄ composites for electromagnetic wave absorption, *Chem. Eng. J.* 393 (2020), 124743.
- [37] X. Lin, K. Shih, J. Chen, X. Xie, Y. Zhang, Y. Chen, Z. Chen, Y. Li, Insight into flower-like greigite-based peroxydisulfate activation for effective bisphenol A abatement: performance and electron transfer mechanism, *Chem. Eng. J.* 391 (2020), 123558.
- [38] Y.J. Choe, J.Y. Byun, S.H. Kim, J. Kim, Fe₃S₄/Fe₇S₈-promoted degradation of phenol via heterogeneous, catalytic H₂O₂ scission mediated by S-modified surface Fe²⁺ species, *Appl. Catal. B: Environ.* 233 (2018) 272–280.
- [39] W. Liu, L. Jin, J. Xu, J. Liu, Y. Li, P. Zhou, C. Wang, R.A. Dahlgren, X. Wang, Insight into pH dependent Cr(VI) removal with magnetic Fe₃S₄, *Chem. Eng. J.* 359 (2018) 564–571.
- [40] N.M. Mahmoodi, J. Abdi, M. Taghizadeh, A. Taghizadeh, B. Hayati, A.A. Shekarchi, M. Vossoughi, Activated carbon/metal-organic framework nanocomposite: preparation and photocatalytic dye degradation mathematical modeling from wastewater by least squares support vector machine, *J. Environ. Manage.* 233 (2019) 660–672.
- [41] Y. Li, J. Li, Y. Pan, Z. Xiong, G. Yao, R. Xie, B. Lai, Peroxymonosulfate activation on FeCo₂S₄ modified g-C₃N₄ (FeCo₂S₄-CN): mechanism of singlet oxygen evolution for nonradical efficient degradation of sulfamethoxazole, *Chem. Eng. J.* 384 (2020), 123361.
- [42] Y. Long, S. Li, Y. Su, S. Wang, S. Zhao, S. Wang, Z. Zhang, W. Huang, Y. Liu, Z. Zhang, Sulfur-containing iron nanocomposites confined in S/N co-doped carbon for catalytic peroxymonosulfate oxidation of organic pollutants: low iron leaching, degradation mechanism and intermediates, *Chem. Eng. J.* 404 (2021), 126499.
- [43] H. Olvera-Vargas, N. Gore-Datar, O. Garcia-Rodriguez, S. Mutnuri, O. Lefebvre, Electro-Fenton treatment of real pharmaceutical wastewater paired with a BDD anode: reaction mechanisms and respective contribution of homogeneous and heterogeneous [•]OH, *Chem. Eng. J.* 404 (2021), 126524.
- [44] Y. Zhang, A. Wang, X. Tian, Z. Wen, H. Lv, D. Li, J. Li, Efficient mineralization of the antibiotic trimethoprim by solar assisted photoelectro-Fenton process driven by a photovoltaic cell, *J. Hazard. Mater.* 318 (2016) 319–328.
- [45] I. Michael, E. Hapeshi, V. Osorio, S. Perez, M. Petrovic, A. Zapata, S. Malato, D. Barceló, D. Fatta-Kassinos, Solar photocatalytic treatment of trimethoprim in four environmental matrices at a pilot scale: transformation products and ecotoxicity evaluation, *Sci. Total Environ.* 430 (2012) 167–173.
- [46] Y. Ji, W. Xie, Y. Fan, Y. Shi, D. Kong, J. Lu, Degradation of trimethoprim by thermo-activated persulfate oxidation: reaction kinetics and transformation mechanisms, *Chem. Eng. J.* 286 (2016) 16–24.
- [47] X. Luo, Z. Zheng, J. Greaves, W.J. Cooper, W. Song, Trimethoprim: kinetic and mechanistic considerations in photochemical environmental fate and AOP treatment, *Water Res.* 46 (2012) 1327–1336.
- [48] N.M. Mahmoodi, M. Arami, N.Y. Limaee, K. Gharanjig, F. Nourmohammadian, Nanophotocatalysis using immobilized titanium dioxide nanoparticle: degradation and mineralization of water containing organic pollutant: case study of Butachlor, *Mater. Res. Bull.* 42 (2007) 797–806.
- [49] F.C. Moreira, S. Garcia-Segura, A.R.B. Rui, E. Brillas, V.J.P. Vilar, Degradation of the antibiotic trimethoprim by electrochemical advanced oxidation processes using a carbon-PTFE air-diffusion cathode and a boron-doped diamond or platinum anode, *Appl. Catal. B: Environ.* 160–161 (2014) 492–505.
- [50] P. Cao, X. Quan, K. Zhao, S. Chen, H. Yu, J. Niu, Selective electrochemical H₂O₂ generation and activation on a bifunctional catalyst for heterogeneous electro-Fenton catalysis, *J. Hazard. Mater.* 382 (2020), 121102.
- [51] Y. Zhu, F. Deng, S. Qiu, F. Ma, Y. Zheng, R. Lian, Enhanced electro-Fenton degradation of sulfonamides using the N, S co-doped cathode: mechanism for H₂O₂ formation and pollutants decay, *J. Hazard. Mater.* 403 (2021), 123950.
- [52] P. Hao, Y. Xin, J. Tian, L. Li, J. Xie, F. Lei, L. Tong, H. Liu, B. Tang, Novel (Ni, Fe) S₂/(Ni, Fe)₃S₄ solid solution hybrid: an efficient electrocatalyst with robust oxygen-evolving performance, *Sci. China Chem.* 63 (2020) 1030–1039.
- [53] P. Huang, L. Yao, Q. Chang, Y. Sha, G. Jiang, S. Zhang, Z. Li, Room-temperature preparation of highly efficient NH₂-MIL-101(Fe) catalyst: the important role of -NH₂ in accelerating Fe(III)/Fe(II) cycling, *Chemosphere* 291 (2021), 133026.
- [54] X. Zhang, B. Xu, S. Wang, X. Li, B. Liu, Y. Xu, P. Yu, Y. Sun, High-density dispersion of Cu_N sites for H₂O₂ activation toward enhanced Photo-Fenton performance in antibiotic contaminant degradation, *J. Hazard. Mater.* 423 (2022), 127039.